INTERNATIONAL JOURNAL FOR NUMERICAL METHODS IN FLUIDS
Int. J. Numer. Meth. Fluids 2008; **57**:951–976
Published online 17 December 2007 in Wiley InterScience (www.interscience.wiley.com). DOI: 10.1002/fld.1668

Raviart–Thomas and Brezzi–Douglas–Marini finite-element approximations of the shallow-water equations

V. Rostand*, † and D. Y. Le Roux

Département de Mathématiques et de Statistique, Université Laval, Québec, QC, Canada G1K 7P4

SUMMARY

An analysis of the discrete shallow-water equations using the Raviart–Thomas and Brezzi–Douglas–Marini finite elements is presented. For inertia–gravity waves, the discrete formulations are obtained and the dispersion relations are computed in order to quantify the dispersive nature of the schemes on two meshes made up of equilateral and biased triangles. A linear algebra approach is also used to ascertain the possible presence of spurious modes arising from the discretization. The geostrophic balance is examined and the smallest representable vortices are characterized on both structured and unstructured meshes. Numerical solutions of two test problems to simulate gravity and Rossby modes are in good agreement with the analytical results. Copyright © 2007 John Wiley & Sons, Ltd.

Received 30 June 2007; Revised 12 October 2007; Accepted 14 October 2007

KEY WORDS: shallow-water equations; finite-element method; dispersion relations; Raviart–Thomas; Brezzi–Douglas–Marini

1. INTRODUCTION

The finite-element (FE) method is attractive for problems of environmental engineering due to the flexibility of triangulation for the representation of irregular boundaries and for local mesh refinement [1–7]. The method is widely applied to shallow-water (SW) simulation for a variety of environmental problems including groundwater, coastal regions, atmospheric flows, and oceanic flows [1, 3, 8–10]. The SW equations describe the behavior of a shallow homogeneous incompressible and inviscid fluid layer. They are derived from the Navier–Stokes equations under Boussinesq and hydrostatic pressure assumptions.

*Correspondence to: V. Rostand, Département de Mathématiques et de Statistique, Université Laval, Québec, QC, Canada G1K 7P4.
†E-mail: vrostand@gmail.com

Contract/grant sponsor: Natural Sciences and Engineering Research Council (NSERC)
Contract/grant sponsor: FQRNT (Fonds Québécois de la Recherche sur la Nature et les Technologies)

One of the key issues that arises with mixed formulations is the possible presence of spurious modes, i.e. small-scale artifacts, introduced by the spatial discretization scheme. This difficulty with mixed methods is encountered in both SW and Navier–Stokes formulations. The appearance of spurious solutions is mainly due to an inappropriate choice of approximation function spaces for the FE method. The spurious modes usually take the form of pressure or surface elevation, velocity, and/or Coriolis modes. They do not propagate but are trapped within the model grid. The spurious solutions usually cause aliasing and an accumulation of energy in the smallest-resolvable scale, leading to noisy solutions. Improvements have been achieved through the use of a variety of mixed-order FE interpolation schemes [3, 5, 9, 11–13], a wave equation formulation [7, 14], and stabilization methods [15].

Dispersion analysis of the discretized form of the linear SW equations is a useful tool to define the relationships between frequency and wave number. It also permits to explicitly ascertain the presence and determine the form of spurious solutions as well as the dispersive/dissipative nature of a FE formulation [16–20]. However, such an approach is restricted to uniform meshes and periodic solutions. In order to study the existence and the behavior of stationary spurious modes associated with zero frequency on both uniform and unstructured meshes, a linear algebra approach may be employed [21, 22]. It consists in determining the properties of the kernel of the associated discretized problem. The kernel characterization may also be used to determine the form of the smallest representative velocity vortex structures that can be represented in a given discretization.

The dispersion analyses and linear algebra approach performed in [18, 19, 22] suggest that three FE schemes, the P_1^{NC}–P_1 and P_0–P_1 pairs and the low-order Raviart–Thomas element RT_0, can be identified as promising schemes in terms of dispersion properties for the discretization of the SW equations. The aim of this paper is to conduct such analyses for higher-order Raviart–Thomas and Brezzi–Douglas–Marini (BDM_1) FE approximation spaces. The BDM_1 element has been introduced in [23] for solving elliptic problems and to our knowledge it is analyzed here for the first time in the context of inviscid SW flows. Two formulations are considered: the BDM_1–P_0 and the BDM_1–P_1 pairs.

The paper is organized as follows. We first present the governing equations and the spatial discretization in Sections 2 and 3, respectively. A dispersion analysis is performed in Section 4 for the inertia–gravity waves. In Section 5, a linear algebra approach based on the kernel properties of the discretized problem is used for Rossby waves. The analytical computations are followed by numerical simulations. Some concluding remarks complete the study.

2. GOVERNING EQUATIONS

Let Ω be a 2D domain with boundary Γ. The inviscid linear equations are expressed in Cartesian coordinates [24] as

$$\frac{\partial \mathbf{u}}{\partial t} + f\mathbf{k}\times\mathbf{u} + g\nabla\eta = 0 \tag{1}$$

$$\frac{\partial \eta}{\partial t} + H\nabla\cdot\mathbf{u} = 0 \tag{2}$$

where $\mathbf{u}=(u, v)$ is the velocity field, η is the surface elevation with respect to the reference level $z=0$, $\mathbf{k}$ is the unit vector pointing in the vertical direction, g denotes the gravitational acceleration,

DOI: 10.1002/fld

and the mean depth H and the Coriolis parameter f are assumed constant, unless otherwise stated. The velocity is subject to the no-normal flow boundary condition $\mathbf{u}\cdot\mathbf{n}=0$ on Γ, where $\mathbf{n}$ is the outward pointing vector at the boundary.

For the analyses performed in this paper, time is assumed continuous and we seek periodical solutions of (1)–(2) of the form

$$\mathbf{u}(x,y,t)=\mathbf{u}(x,y)\exp(\mathrm{i}\omega t),\quad \eta(x,y,t)=\eta(x,y)\exp(\mathrm{i}\omega t) \tag{3}$$

where ω is the angular frequency.

By substituting (3) in (1) and (2) we obtain

$$\mathrm{i}\omega\mathbf{u}+f\mathbf{k}\times\mathbf{u}+g\nabla\eta=0 \tag{4}$$

$$\mathrm{i}\omega\eta+H\nabla\cdot\mathbf{u}=0 \tag{5}$$

Equations (4) and (5) are now discretized in space.

3. SPATIAL DISCRETIZATION

3.1. The weak formulation

We assume that $\mathbf{u}$ and η belong to the spaces $\mathbf{V}$ and W, with $\mathbf{V}$ and W in the square-integrable space $L^2(\Omega)$. The weak formulation is obtained by multiplying (4) and (5) by test functions $\boldsymbol{\varphi}$ and ψ belonging to $\mathbf{V}$ and W, respectively, and by integrating over the whole domain:

$$\int_\Omega \mathrm{i}\omega\mathbf{u}\cdot\boldsymbol{\varphi}\,\mathrm{d}\mathbf{x}+\int_\Omega f(\mathbf{k}\times\mathbf{u})\cdot\boldsymbol{\varphi}\,\mathrm{d}\mathbf{x}+\int_\Omega g\nabla\eta\cdot\boldsymbol{\varphi}\,\mathrm{d}\mathbf{x}=0\quad\forall\boldsymbol{\varphi}\in\mathbf{V} \tag{6}$$

$$\int_\Omega \mathrm{i}\omega\eta\psi\,\mathrm{d}\mathbf{x}+\int_\Omega H\nabla\cdot\mathbf{u}\psi\,\mathrm{d}\mathbf{x}=0\quad\forall\psi\in W \tag{7}$$

where $\mathrm{d}\mathbf{x}$ is the area element with $\mathbf{x}=(x,y)$. The terms containing gradient and divergence operators in (6) and (7) may be integrated by parts using Green's theorem depending on the regularity of spaces $\mathbf{V}$ and W.

3.2. Galerkin FE discretization

The Galerkin method approximates the solution of (6) and (7) in finite-dimensional subspaces. Consider a representative meshlength parameter h that measures resolution and a FE triangulation $\mathscr{T}_h$ of the polygonal domain Ω.

The discrete solutions $\mathbf{u}_h$ and η_h sought belong to finite-dimensional spaces $\mathbf{V}_h$ and W_h, respectively, with $\dim(\mathbf{V}_h)=p$ and $\dim(W_h)=q$. The spaces $\mathbf{V}_h$ and W_h are defined as a set of piecewise polynomial functions over the triangulation $\mathscr{T}_h$. The degree and continuity order of these polynomial functions are specified in the sequel for the FE schemes investigated in this paper.

The components of $\mathbf{u}_h$ and η_h are represented over a triangle K by interpolating functions $\varphi(x,y)$ and $\psi(x,y)$, belonging to $\mathbf{V}_h$ and W_h, respectively. We thus have

$$\mathbf{u}_h=\sum_{j=1}^{p}\mathbf{u}_j\varphi_j,\quad \eta_h=\sum_{k=1}^{q}\eta_k\psi_k \tag{8}$$

DOI: 10.1002/fld

Note that for the RT_0 and BDM_1 elements, the normal velocities are expressed in terms of the vector interpolating function $\boldsymbol{\varphi}(x, y)$.

Let $\underline{M}$ and $\underline{N}$ be the velocity and elevation mass matrices, respectively, $\underline{C}$ the Coriolis matrix, and $\underline{G}$ and $\underline{D}$ the gradient and divergence matrices, which are obtained from the elementary matrices

$$\begin{aligned} \underline{M}_{j_1,j_2} &= \mathrm{i}\omega \int_\Omega \boldsymbol{\varphi}_{j_1} \cdot \boldsymbol{\varphi}_{j_2}, \quad \underline{N}_{k_1,k_2} = \mathrm{i}\omega \int_\Omega \psi_{k_1} \psi_{k_2}, \quad \underline{C}_{j_1,j_2} = \int_\Omega f(\mathbf{k} \times \boldsymbol{\varphi}_{j_1}) \cdot \boldsymbol{\varphi}_{j_2} \\ \underline{D}_{k_1,j_1} &= \int_\Omega H(\nabla \cdot \boldsymbol{\varphi}_{j_1}) \psi_{k_1}, \quad \underline{G}_{j_1,k_1} = \int_\Omega g \nabla \psi_{k_1} \cdot \boldsymbol{\varphi}_{j_1} \end{aligned} \tag{9}$$

where $j_1, j_2 = \{1, \ldots, p\}$ and $k_1, k_2 = \{1, \ldots, q\}$. By using (8) and (9), Equations (6) and (7) are rewritten in matrix form as

$$\begin{pmatrix} \underline{M} + \underline{C} & \underline{G} \\ \underline{D} & \underline{N} \end{pmatrix} \begin{pmatrix} \underline{\mathbf{u}} \\ \underline{\eta} \end{pmatrix} = 0 \tag{10}$$

where $\underline{\mathbf{u}} = (u_1, \ldots, u_p)^{\mathrm{t}}$ and $\underline{\eta} = (\eta_1, \ldots, \eta_q)^{\mathrm{t}}$.

3.3. *The* BDM_1 *element*

The BDM_1 element has been introduced by Brezzi *et al.* [23] in 1986 to solve elliptic problems. It can be seen as an enriched version of the lowest-order Raviart–Thomas element denoted by RT_0. The RT_0 element is based on flux conservation on element edges and it has continuous normal components at triangle midedge points. For the BDM_1 element, the normal component is continuous through triangle edges, as for the RT_0 element, but the corresponding basis functions are linear instead of being constant. Consequently, the BDM_1 element has two degrees of freedom over each triangle side instead of one for the RT_0 element.

Consider a triangle K of $\mathscr{T}_h$ and let $\mathbf{x}_i = (x_i, y_i)$, $i = 1, 2, 3$, be the coordinates of the three vertices of K. At each side of K the tangential and normal vectors are defined as

$$\begin{aligned} \mathbf{t}_1 &:= \mathbf{x}_3 - \mathbf{x}_2, \quad \mathbf{n}_1 := -\mathbf{k} \times \mathbf{t}_1 \\ \mathbf{t}_2 &:= \mathbf{x}_1 - \mathbf{x}_3, \quad \mathbf{n}_2 := -\mathbf{k} \times \mathbf{t}_2 \\ \mathbf{t}_3 &:= \mathbf{x}_2 - \mathbf{x}_1, \quad \mathbf{n}_3 := -\mathbf{k} \times \mathbf{t}_3 \end{aligned} \tag{11}$$

Let λ_i, $i = 1, 2, 3$, be the barycentric functions of K and define for each permutation (ijk) of (123) the basis functions $\boldsymbol{\varphi}$ associated with the BDM_1 element

$$\boldsymbol{\varphi}_{(ijk)} := \frac{\lambda_j \mathbf{t}_k}{\mathbf{t}_k \cdot \mathbf{n}_i} = \frac{\lambda_j \mathbf{t}_k}{2\,\mathrm{Area}(K)} (-1)^{\mathrm{sgn}(ijk)} \tag{12}$$

where $\mathrm{Area}(K)$ denotes the area of triangle K. By using (12), one can verify that the normal component $\boldsymbol{\varphi}_{(ijk)} \cdot \mathbf{n}$ is linear on edge i and zero on edges j and k. Further, on edge i the normal component takes the value 1 at vertex j and 0 at vertex k. In order to simplify the notation, the

DOI: 10.1002/fld

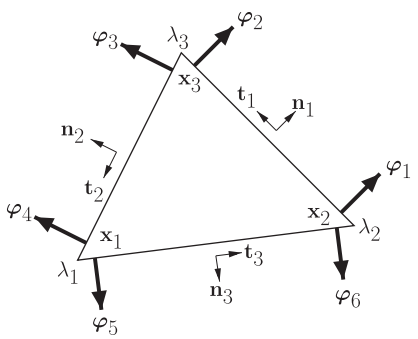

Figure 1. Elementary basis functions for the BDM_1 space.

functions $\boldsymbol{\varphi}$ are numbered from 1 to 6

$$\begin{aligned} &\boldsymbol{\varphi}_1 := \boldsymbol{\varphi}_{(123)}, \quad \boldsymbol{\varphi}_2 := \boldsymbol{\varphi}_{(132)}, \quad \boldsymbol{\varphi}_3 := \boldsymbol{\varphi}_{(231)} \\ &\boldsymbol{\varphi}_4 := \boldsymbol{\varphi}_{(213)}, \quad \boldsymbol{\varphi}_5 := \boldsymbol{\varphi}_{(312)}, \quad \boldsymbol{\varphi}_6 := \boldsymbol{\varphi}_{(321)} \end{aligned} \tag{13}$$

in terms of permutations, as shown in Figure 1. Note that on each triangle edge of K the sum of the two basis functions $\boldsymbol{\varphi}$ exactly corresponds to the basis function associated with the RT_0 element on that edge.

3.4. FE pairs

As previously mentioned, one of the issues associated with mixed methods is the possibility of spurious modes and anomalous dispersion in the representation of waves. The choice of FE pairs to approximate the velocity field $\mathbf{u}$ and the surface elevation η is thus delicate. In [18, 19, 22] three FE pairs, namely the P_1^{NC}–P_1 and P_0–P_1 pairs and the low-order Raviart–Thomas element RT_0, have been identified as promising schemes in terms of dispersion properties for the discretization of the SW equations. Common to the first two FE velocity/surface-elevation pairs is a piecewise-linear continuous representation of surface elevation, and they differ from one another in their representation of velocity. The P_1^{NC}–P_1 pair [3, 17] has velocity nodes at triangle edge midpoints, and linear basis functions are used to approximate the two velocity components on the element's two-triangle support. Since this particular representation of velocity is continuous only across triangle boundaries at midpoint nodes and discontinuous everywhere else around a triangle boundary, this element is termed nonconforming (NC) in the FE literature. The P_0–P_1 pair has a piecewise-constant representation of velocity. In [18, 19, 22] the RT_0 element has a discontinuous piecewise-constant representation of surface elevation and such a FE pair is thus named RT_0–P_0 in the sequel.

The purpose of this paper is to study the dispersive properties and eventually detect the presence of spurious modes of three other FE pairs. Those are the RT_0–P_1, BDM_1–P_0, and BDM_1–P_1 pairs. The RT_0–P_1 pair has RT_0 basis functions for velocity and a piecewise-linear continuous representation of surface elevation. Common to the last two pairs is a BDM_1 representation of velocity and the corresponding basis functions for elevation are piecewise constant and piecewise linear, respectively.

DOI: 10.1002/fld

4. INERTIA–GRAVITY WAVES

4.1. Analytical frequencies

In the continuum case the free modes of (4) and (5) are examined by perturbing about the basic state $u=v=\eta=0$. We seek periodic solutions of the form

$$(\mathbf{u}(x,y),\eta(x,y))=(\tilde{\mathbf{u}},\tilde{\eta})\exp(\mathrm{i}(kx+ly)) \tag{14}$$

where k and l are the wave numbers in the x- and y-directions, respectively. Substitution into (4) and (5) leads to a square matrix system for the amplitudes $\tilde{\mathbf{u}}$ and $\tilde{\eta}$. For a nontrivial solution to exist, the 3×3 determinant of the matrix must equal zero, and this constraint leads to the following dispersion relation for the frequency:

$$\omega(\omega^2-f^2-gH\sqrt{k^2+l^2})=0 \tag{15}$$

The first solution $\omega=0$ is the geostrophic mode and would correspond to the slow Rossby mode on a β-plane, while the other two solutions

$$\omega_{\mathrm{AN}}=\pm\sqrt{f^2+gH(k^2+l^2)} \tag{16}$$

correspond to the free-surface gravitational modes with rotational correction. Since ω is purely real, all modes are neutrally stable and neither amplify nor decay.

4.2. Discrete frequencies

The dispersion analysis is performed on two types of regular meshes: Meshes 1 and 2. Mesh 1 corresponds to equilateral triangles and Mesh 2 is made up of biased right isosceles triangles as shown in Figure 10. The mesh spacing, denoted by h, is defined as the triangle side length for Mesh 1 and the shortest triangle side length for Mesh 2.

Nodal unknowns are located on typical nodal sets, e.g. faces, vertices, and barycenters. In this analysis only selected discrete equations are retained and they correspond to each type of nodes. For example, three discrete momentum equations are considered for the RT_0–P_0 pair on the three possible types of faces, and two discrete continuity equations are considered at the two possible types of barycenters, e.g. upward and downward pointing triangles as shown in Figure 3 for Mesh 1. Consequently, selected discrete amplitudes $\tilde{u}_j$ and $\tilde{\eta}_j$ are considered for each nodal set. Assembling the elementary matrices defined in (9) leads to the stencils of Figures 4–7 for the P_1^{NC}–P_1, RT_0–P_0, RT_0–P_1, BDM_1–P_0, and BDM_1–P_1 pairs. Substitution of (14) in these reference stencils leads to the linear system

$$\begin{pmatrix} M+C & G \\ D & N \end{pmatrix}\begin{pmatrix} \tilde{\mathbf{u}} \\ \tilde{\eta} \end{pmatrix}=0 \tag{17}$$

where $\tilde{\mathbf{u}}$ and $\tilde{\eta}$ are the amplitude vectors. Matrices M, N, C, D, and G are the contributions of velocity mass, surface-elevation mass, Coriolis, divergence, and gradient stencils, respectively, for the selected equations. As for the continuous case, the determinant of the matrix in the left-hand

DOI: 10.1002/fld

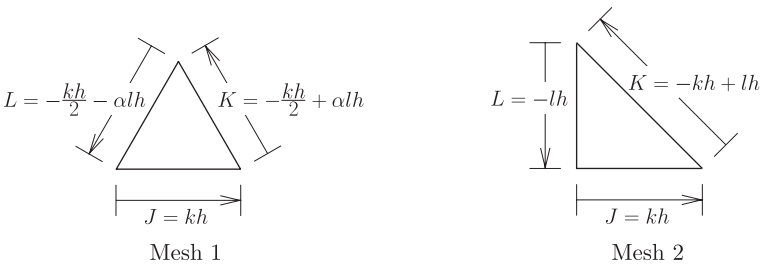

Figure 2. Elementary displacements are represented on the reference triangle on Meshes 1 and 2.

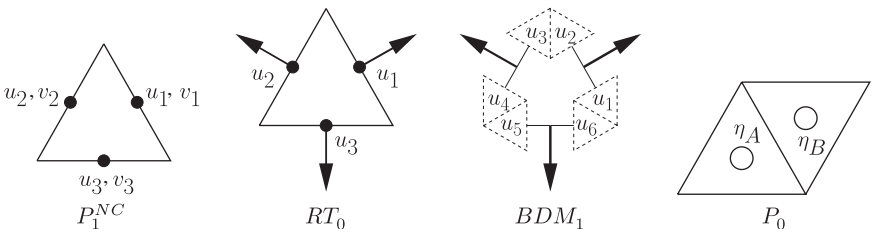

Figure 3. Discrete amplitude numbering for the P_1^{NC}, RT_0, BDM_1, and P_0 elements.

side of (17) must vanish to admit nontrivial amplitude solutions, and this leads to the dispersion relation. Note that we have

$$G=-\frac{g}{H}\overline{D^{\mathrm{t}}} \tag{18}$$

where $\overline{D^{\mathrm{t}}}$ is the complex conjugate transpose of D. Consequently, only divergence stencils are displayed in the following. To simplify the notation, we define the quantities J, K, and L as elementary displacements as shown in Figure 2 on Meshes 1 and 2. Note that J, K, and L are different on both meshes. Further, we let I_n be the $n\times n$ identity matrix and $\alpha=\sqrt{3}/2$.

We now examine the dispersion relations corresponding to the FE pairs considered in this study.

4.2.1. The P_1^{NC}–P_1 pair. The discrete velocity amplitudes are considered on three typical faces (see Figure 3) and ordered as

$$\tilde{\mathbf{u}}=(\tilde{u}_1,\tilde{u}_2,\tilde{u}_3,\tilde{v}_1,\tilde{v}_2,\tilde{v}_3)^{\mathrm{t}} \tag{19}$$

Because the P_1^{NC} basis functions are orthogonal in L^2, the velocity mass and Coriolis matrices are block diagonal. For Mesh 1, we obtain from (9)

$$M=\mathrm{i}\omega\frac{\alpha h^2}{3}I_6,\quad C=f\frac{\alpha h^2}{3}N\begin{pmatrix}0 & -I_3\\ I_3 & 0\end{pmatrix} \tag{20}$$

DOI: 10.1002/fld

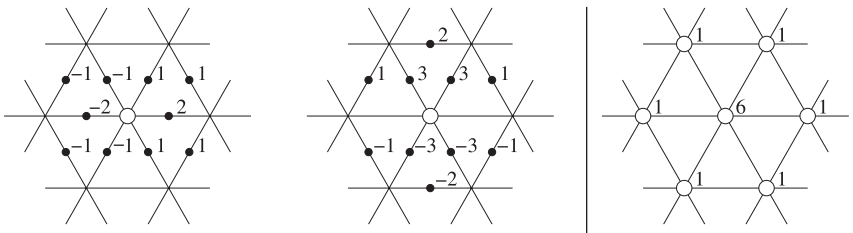

Figure 4. P_1^{NC}–P_1 divergence and P_1 mass stencils.

For the surface elevation, only one discrete amplitude is required for $\tilde{\eta}$ at mesh vertices. The stencils of the divergence operator in $x-$ and $y-$ directions are shown in Figure 4 and the corresponding matrix is

$$D = H\frac{h}{6}(D_1 \;\; D_2 \;\; D_3 \;\; D_4 \;\; D_5 \;\; D_6) \tag{21}$$

where

$$\begin{aligned}
D_1 &= 2\mathrm{i}\alpha\left(\sin\left(\frac{J-L}{2}\right)+\sin\left(\frac{-K}{2}\right)\right), \quad & D_4 &= \mathrm{i}\left(\sin\left(\frac{J-L}{2}\right)+3\sin\left(\frac{K}{2}\right)\right)\\
D_2 &= 2\mathrm{i}\alpha\left(\sin\left(\frac{J-K}{2}\right)+\sin\left(\frac{-L}{2}\right)\right), \quad & D_5 &= \mathrm{i}\left(\sin\left(\frac{J-K}{2}\right)+3\sin\left(\frac{L}{2}\right)\right)\\
D_3 &= 4\mathrm{i}\alpha\sin\left(\frac{J}{2}\right), & D_6 &= 2\mathrm{i}\sin\left(\frac{K-L}{2}\right)
\end{aligned} \tag{22}$$

The mass stencil for the P_1 elevation is shown in Figure 4 and the corresponding matrix is

$$\begin{aligned}
N &= \mathrm{i}\omega\frac{\alpha h^2}{12}(6+\mathrm{e}^{\mathrm{i}J}+\mathrm{e}^{\mathrm{i}L}+\mathrm{e}^{\mathrm{i}K}+\mathrm{e}^{-\mathrm{i}J}+\mathrm{e}^{-\mathrm{i}L}+\mathrm{e}^{-\mathrm{i}K})\\
&= \mathrm{i}\omega\frac{\alpha h^2}{6}(3+\cos(J)+\cos(K)+\cos(L))
\end{aligned} \tag{23}$$

Vanishing the 7×7 determinant leads to

$$\omega_{1,2} = \pm\omega_{\mathrm{AN}} + O(h^4), \quad \omega_3 = 0, \quad \omega_{4,5,6,7} = \pm f \text{ (double root)}$$

The first two roots $\omega_{1,2}$ correspond to inertia–gravity waves and they coincide with the analytical solution (16) in the limit as mesh spacing $h \to 0$. The third root ω_3 corresponds to the geostrophic mode and $\omega_{4,5,6,7}$ represent spurious propagating inertial oscillations that have no particular spatial characteristics [17, 18]. The dispersion relation on Mesh 2 is given in [17, 18], and the frequency corresponding to inertia–gravity waves is found to be the same order $O(h^4)$.

DOI: 10.1002/fld

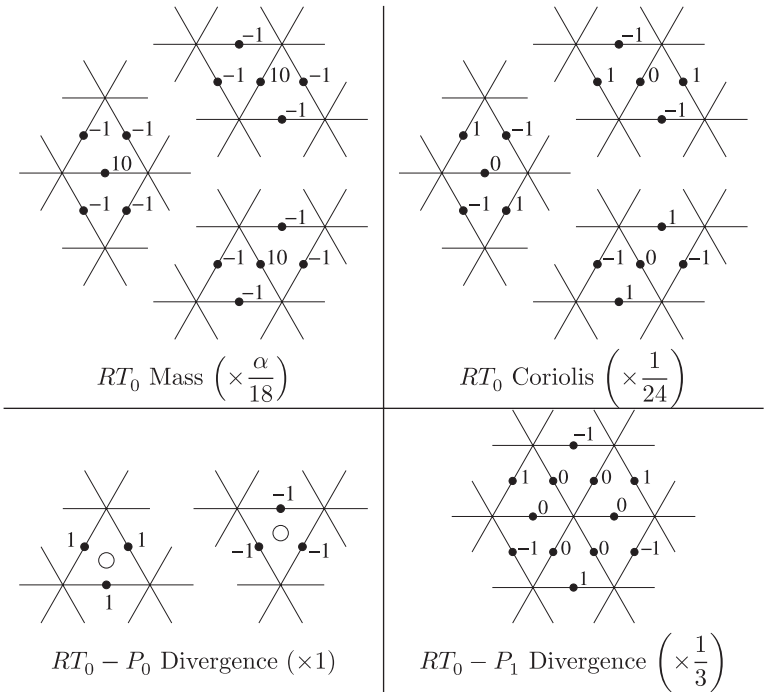

Figure 5. Stencils for the RT_0–P_0 and RT_0–P_1 pairs.

4.2.2. The RT_0–P_0 *pair.* The dispersion relation for the RT_0–P_0 pair on Mesh 2 is given in [18] and the results on Mesh 1 are computed here. By using the notations of Figure 3 the following discrete amplitudes are considered:

$$\tilde{\mathbf{u}} = (\tilde{u}_1, \tilde{u}_2, \tilde{u}_3)^{\mathrm{t}}, \quad \tilde{\eta} = (\tilde{\eta}_A, \tilde{\eta}_B)^{\mathrm{t}} \tag{24}$$

where A and B represent typical barycenters of upward and downward pointing triangles. The velocity mass, Coriolis, and divergence stencils are shown in Figure 5, and the corresponding matrices are

$$M = \mathrm{i}\omega\frac{\alpha}{9}\begin{pmatrix} 5 & -\cos\left(\frac{J}{2}\right) & -\cos\left(\frac{L}{2}\right) \\ -\cos\left(\frac{J}{2}\right) & 5 & -\cos\left(\frac{K}{2}\right) \\ -\cos\left(\frac{L}{2}\right) & -\cos\left(\frac{K}{2}\right) & 5 \end{pmatrix} \tag{25}$$

DOI: 10.1002/fld

$$C = f\frac{1}{3}\begin{pmatrix} 0 & -\cos\left(\frac{J}{2}\right) & \cos\left(\frac{L}{2}\right) \\ \cos\left(\frac{J}{2}\right) & 0 & -\cos\left(\frac{K}{2}\right) \\ -\cos\left(\frac{L}{2}\right) & \cos\left(\frac{K}{2}\right) & 0 \end{pmatrix} \tag{26}$$

$$D = H\begin{pmatrix} E\left(\frac{J-L}{6}\right) & E\left(\frac{K-J}{6}\right) & E\left(\frac{L-K}{6}\right) \\ -E\left(\frac{L-J}{6}\right) & -E\left(\frac{J-K}{6}\right) & -E\left(\frac{K-L}{6}\right) \end{pmatrix} \tag{27}$$

$$N = \mathrm{i}\omega\frac{\alpha h^2}{2}I_2 \tag{28}$$

where $E(X) = \exp(\mathrm{i}X)$. For example, the mass stencil for the RT_0 element is shown in Figure 5 and at node 1 (see Figure 3) we obtain

$$\frac{\alpha}{18}(10\tilde{u}_1 - (\mathrm{e}^{\mathrm{i}J/2} + \mathrm{e}^{-\mathrm{i}J/2})\tilde{u}_2 - (\mathrm{e}^{\mathrm{i}L/2} + \mathrm{e}^{-\mathrm{i}L/2})\tilde{u}_3)$$

which corresponds to the first line of M in (25).

For the 5×5 determinant to vanish we obtain

$$\omega_{1,2} = \pm\omega_{\mathrm{AN}} + O(h^2), \quad \omega_3 = 0, \quad \omega_{4,5} = O(h^{-1})$$

for infinitesimal mesh spacing.

4.2.3. The RT_0–P_1 *pair.* Common to the RT_0–P_0 and RT_0–P_1 is an RT_0 representation of the velocity and they differ from one another in their representation of elevation. Consequently, the M and C matrices are given by (25) and (26), respectively. As for the P_1^{NC}–P_1 pair, only one discrete amplitude is required for $\tilde{\eta}$ at mesh vertices and hence N is given by (23). The divergence stencil on Mesh 1 is shown in Figure 5 and the D matrix is obtained as

$$D = H\frac{2\mathrm{i}}{3}\begin{pmatrix} \sin\left(\frac{J-L}{2}\right) & \sin\left(\frac{K-J}{2}\right) & \sin\left(\frac{L-K}{2}\right) \end{pmatrix} \tag{29}$$

Vanishing the 4×4 determinant leads to

$$\omega_{1,2} = \pm\omega_{\mathrm{AN}} + O(h^2), \quad \omega_{3,4} = 0 \text{ (double root)}$$

for infinitesimal mesh spacing. For Mesh 2, M and N are found in [18] and C and D are deduced from (26) and (29) by using $J = kh$, $K = -kh + lh$, and $L = -lh$ as in Figure 2. We obtain $\omega_{3,4} = 0$ and $\omega_{1,2}$ again coincides with ω_{AN} for infinitesimal mesh spacing.

DOI: 10.1002/fld

4.2.4. The BDM_1–P_0 *pair.* By using the notations of Figure 3, the following discrete amplitudes are considered:

$$\tilde{\mathbf{u}}=(\tilde{u}_1,\ldots,\tilde{u}_6)^{\mathrm{t}},\quad \tilde{\eta}=(\eta_A,\eta_B)^{\mathrm{t}} \tag{30}$$

After long and tedious algebra, we obtain from stencils of Figures 6 and 7 on Meshes 1 and 2

$$M=\mathrm{i}\omega\frac{\alpha}{36}\begin{pmatrix} M_1(K) & M_2(J,K,L) & M_2(L,K,J)\\ M_2(J,L,K) & M_1(L) & M_2(K,L,J)\\ M_2(L,J,K) & M_2(K,J,L) & M_1(J)\end{pmatrix} \tag{31}$$

$$C=f\frac{1}{24}\begin{pmatrix} 0 & -C_1(K,L) & C_1(K,J)\\ C_1(L,K) & 0 & -C_1(L,J)\\ -C_1(J,K) & C_1(J,L) & 0\end{pmatrix} \tag{32}$$

$$D=H\tfrac{1}{2}(D_1(J,K,L)\;\; D_1(K,L,J)\;\; D_1(L,J,K)) \tag{33}$$

where

$$M_1(J)=\begin{pmatrix} 8 & 2E(J)\\ 2E(-J) & 8\end{pmatrix}$$

$$M_2(J,K,L)=\begin{pmatrix} -E(K)-E(-L) & 2-2E(-J)\\ 2-2E(J) & -E(-K)-E(L)\end{pmatrix}$$

$$C_1(K,L)=\begin{pmatrix} E(K)+E(-L) & 2\\ 2 & E(-K)+E(L)\end{pmatrix}$$

$$D_1(J,K,L)=\begin{pmatrix} -E\left(\dfrac{L-K}{3}\right) & -E\left(\dfrac{K-J}{3}\right)\\ E\left(\dfrac{J-K}{3}\right) & E\left(\dfrac{K-L}{3}\right)\end{pmatrix}$$

For example, the mass stencil for the BDM_1 element is shown in Figure 6 and at node 1 (see Figure 3) we obtain

$$\frac{\alpha}{36}(8\tilde{u}_1+2\mathrm{e}^{\mathrm{i}K}\tilde{u}_2+(-\mathrm{e}^{\mathrm{i}K}-\mathrm{e}^{-\mathrm{i}L})\tilde{u}_3+(2-2\mathrm{e}^{-\mathrm{i}J})\tilde{u}_4+(-\mathrm{e}^{-\mathrm{i}J}-\mathrm{e}^{\mathrm{i}K})\tilde{u}_5+(2-2\mathrm{e}^{-\mathrm{i}L})\tilde{u}_6)$$

which corresponds to the first line of M in (31).

As for the RT_0–P_0, the matrix N is given by (28). On Mesh 2 we obtain

$$M=\mathrm{i}\omega\frac{1}{24}\begin{pmatrix} M_3 & M_5(K,J) & M_5(K,L)\\ M_5(-K,J) & M_4(L) & M_6(J,K,L)\\ M_5(-K,L) & M_6(L,K,J) & M_4(J)\end{pmatrix} \tag{34}$$

DOI: 10.1002/fld

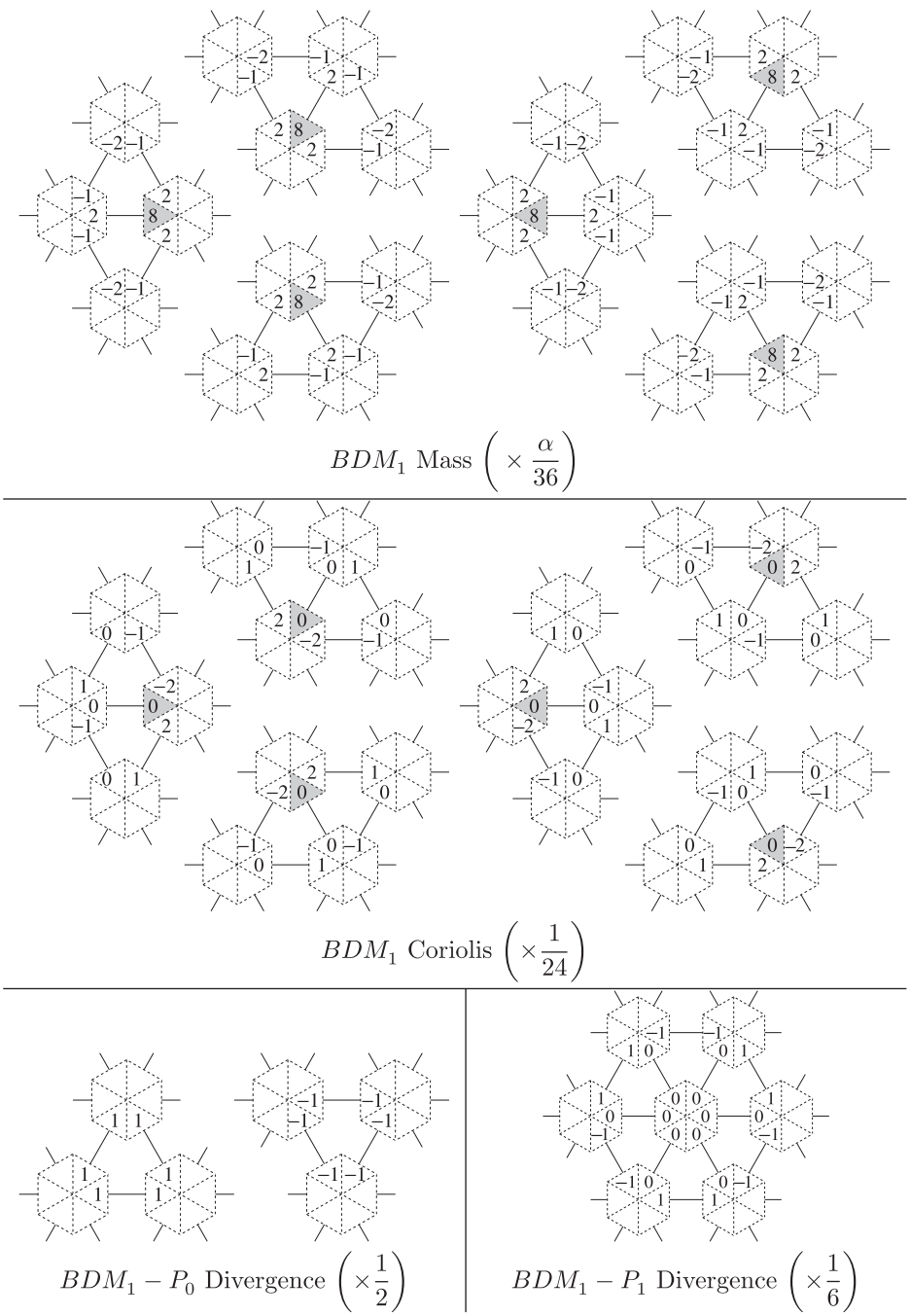

Figure 6. Stencils for the BDM$_1$–P_0 and BDM$_1$–P_1 pairs on Mesh 1.

DOI: 10.1002/fld

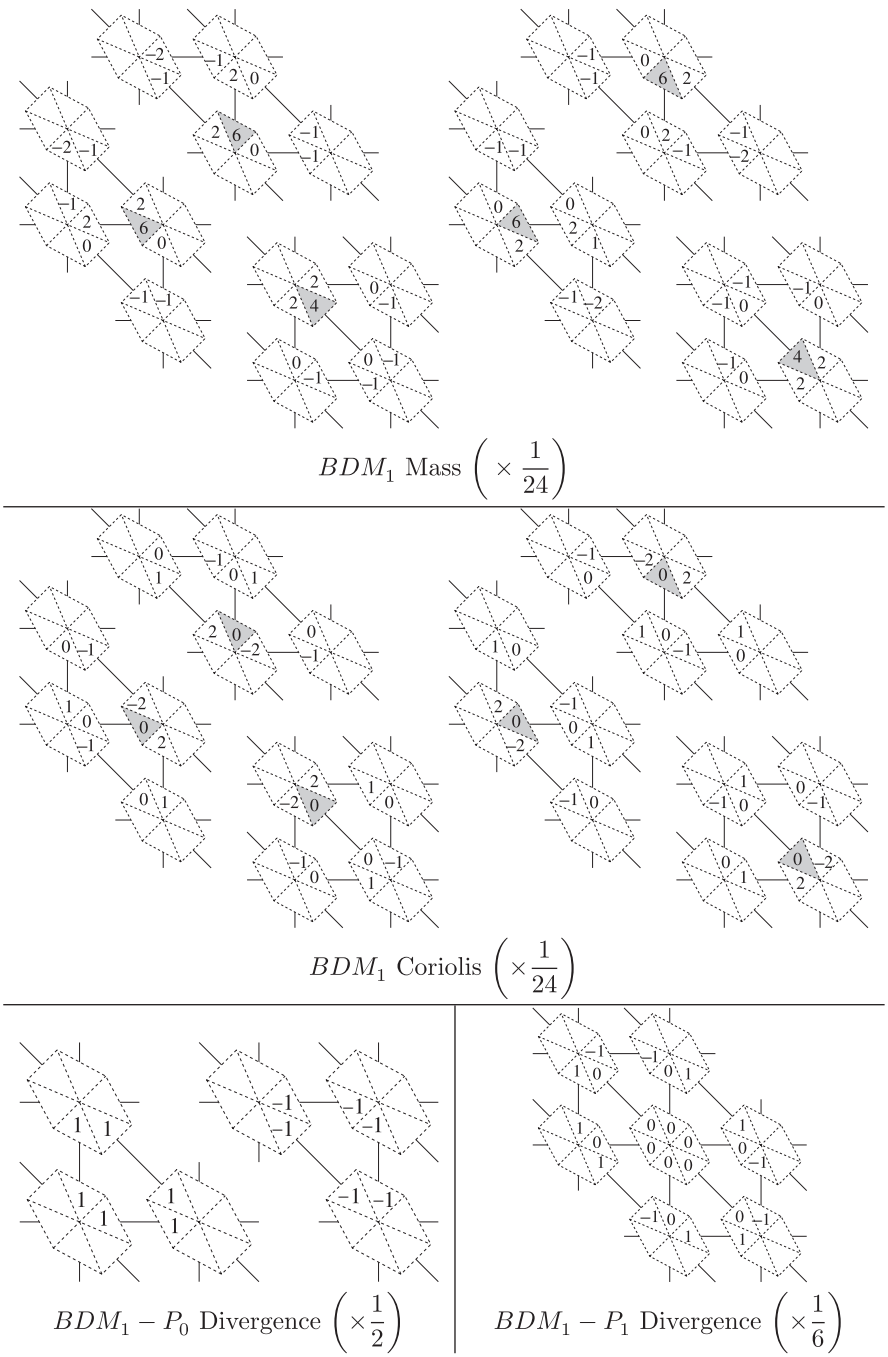

Figure 7. As for Figure 6 but on Mesh 2.

DOI: 10.1002/fld

where

$$M_3 = 4I_2, \qquad M_5(K,J) = \begin{pmatrix} -E(K) & 2-E(-J) \\ 2-E(J) & -E(-K) \end{pmatrix}$$

$$M_4(L) = \begin{pmatrix} 6 & 2E(L) \\ 2E(-L) & 6 \end{pmatrix}, \quad M_6(J,K,L) = \begin{pmatrix} -E(L)-E(-J) & -2E(-K) \\ -2E(K) & -E(-L)-E(J) \end{pmatrix}$$

For Mesh 2, C and D are deduced from (32) and (33) by using the values of J, K, and L as in Figure 2. For the 8×8 determinant to vanish we obtain

$$\omega_{1,2} = \pm\omega_{\mathrm{AN}} + O(h^2), \quad \omega_{3,4,5,6} = 0 \text{ (quadruple root)}, \quad \omega_{7,8} = O(h^{-1})$$

for both meshes and infinitesimal mesh spacing.

4.2.5. The BDM_1–P_1 *pair.* Common to the BDM_1–P_0 and BDM_1–P_1 is a BDM_1 representation of the velocity and they differ from one another in their representation of elevation. Consequently, the M and C matrices are given by (31), (34), and (32). As for the P_1^{NC}–P_1 pair, only one discrete amplitude is required for $\tilde{\eta}$ at mesh vertices and hence N is given by (23). The divergence stencils on Meshes 1 and 2 are found in Figures 6 and 7 and the D matrix is expressed as

$$D = \frac{1}{6h}(D_1(J,L) \;\; D_1(K,J) \;\; D_1(L,K)) \tag{35}$$

where

$$D_1(J,L) = (E(J)-E(L) \;\; E(-L)-E(-J))$$

For both meshes, vanishing the 7×7 determinant leads to

$$\omega_{1,2} = \pm\omega_{\mathrm{AN}} + O(h^4), \quad \omega_{3,4,5} = 0 \text{ (triple root)}, \quad \omega_{6,7} = O(h^2)$$

We note that similar to the P_1^{NC}–P_1 pair the discrete inertia–gravity wave frequencies are computed very accurately ($O(h^4)$) for infinitesimal mesh spacing.

4.3. Summary of discrete frequencies

The previous results are summarized in Table I, where n is the dimension of the linear system (17), and hence the degree of the dispersion relation for the five FE pairs examined here. We mention the multiplicity of the discrete frequency types and the order of accuracy for inertia–gravity waves. For infinitesimal mesh spacing ($h\to 0$) we have $\omega_{1,2}\to\omega_{\mathrm{AN}}$ for all schemes and hence discrete inertia–gravity frequencies are consistent with the continuous case. The slow mode corresponding to $\omega = 0$ is present for all pairs. However, for the RT_0–P_1, BDM_1–P_0, and BDM_1–P_1 pairs, the multiplicity of this mode is greater than 1. Further, a $O(h^2)$ mode exists for the BDM_1–P_1 pair. We also observe the presence of solutions of the form $\omega = \pm f$ for the P_1^{NC}–P_1 pair. These modes usually arise when the discrete scheme involves more velocity nodes than surface-elevation nodes [17, 18]. They are propagating spurious inertial oscillations that have no particular spatial characteristics. Finally, the FE pairs having a discontinuous representation of surface elevation have spurious frequencies of type $O(h^{-1})$ as in [16, 18].

DOI: 10.1002/fld

Table I. Multiplicity of the discrete frequencies obtained from the dispersion relations for the five FE pairs examined in Section 4.2.

FE pair	n	$\omega=\pm\omega_{AN}$	$\omega=0$	$\omega=\pm f$	$\omega=O(h^{-1})$	$\omega=O(h^2)$
$P_1^{NC}-P_1$	7	$2:O(h^4)$	1	4	0	0
RT_0-P_0	5	$2:O(h^2)$	1	0	2	0
RT_0-P_1	4	$2:O(h^2)$	2	0	0	0
BDM_1-P_0	8	$2:O(h^2)$	4	0	2	0
BDM_1-P_1	7	$2:O(h^4)$	3	0	0	2

4.4. Gravity wave limit of discrete frequencies

We now analyze the computed frequencies $\omega_{CP}\equiv\omega_{1,2}$ for the five FE pairs examined in Section 4.2. Because the Coriolis factor does not have a significant impact on the propagation of gravity waves we let $f=0$ to obtain the gravity wave limit. From (16) and the results of Section 4.2, we determine the analytical and computed phase speeds, denoted by c_{AN} and c_{CP}, respectively,

$$c_{AN}\equiv\frac{\omega_{AN}}{\sqrt{k^2+l^2}}=\pm\sqrt{gH},\quad c_{CP}\equiv\frac{\omega_{CP}}{\sqrt{k^2+l^2}}$$

The phase speed ratio, denoted by r_{PH}, is then computed as the ratio of the computed phase speed to the analytical one, with

$$r_{PH}\equiv\left|\frac{c_{CP}}{c_{AN}}\right|=\left|\frac{\omega_{CP}}{\omega_{AN}}\right|=\frac{|\omega_{CP}|}{\sqrt{gH(k^2+l^2)}} \tag{36}$$

Note that we should have $r_{PH}=1$ in the absence of numerical dispersion. We show r_{PH} as a surface function depending on the normalized wave numbers kh and lh for Meshes 1 and 2 in Figure 8. The values of kh and lh for Mesh 1 vary between $\pm4\pi/3$ and $\pm\pi/\alpha$, respectively, in order to include the six points defined later in (37). For Mesh 2, kh and lh vary between $\pm\pi$ as in [18, 25]. The phase advance (r_{PH}) is also plotted in Figure 9 along the selected axes OE and OT for Mesh 1 and OX, OD1, and OD2 for Mesh 2. The directions of these axes are defined in Figure 8 and Table II. For symmetrical reasons the phase advance surfaces are shown only for positive wave numbers in Figure 9.

For the RT_0-P_0 pair we obtain $r_{PH}\leqslant1$ on Mesh 1 for all values of kh and lh and the waves do not accelerate on Mesh 1. On Mesh 2, we have $r_{PH}\leqslant1$ in the OX and OD1 directions but this is not the case in the OD2 direction since the maximum value observed for r_{PH} is 1.18. The $P_1^{NC}-P_1$ pair behaves similarly although a weak acceleration ($r_{PH}=1.02$) is noticeable in the OT, OX, and OD1 directions. For larger wave numbers the RT_0-P_0 and $P_1^{NC}-P_1$ pairs present less dispersion effects than the three other ones examined in Section 4.2 because r_{PH} is closer to 1 for those pairs.

DOI: 10.1002/fld

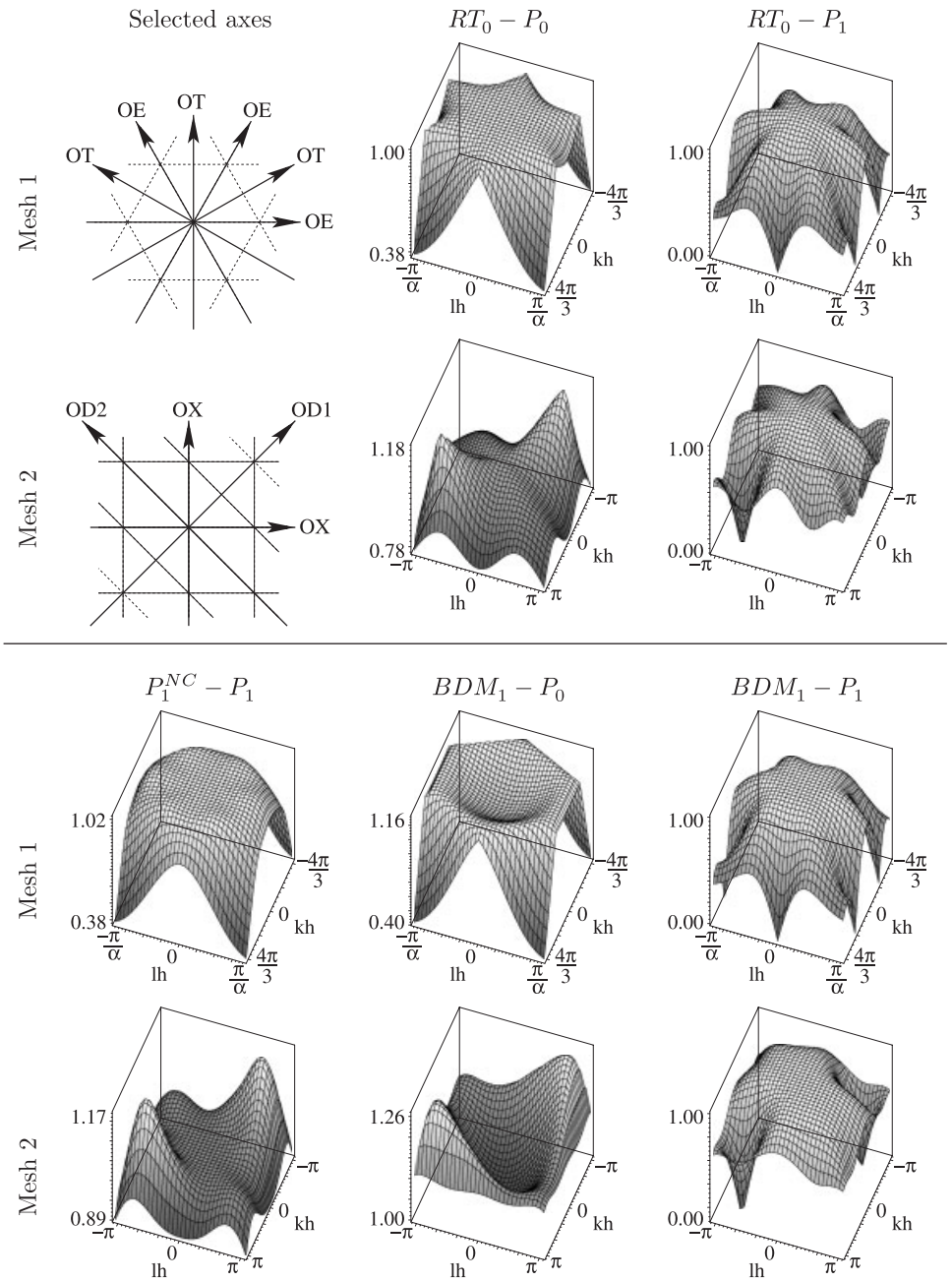

Figure 8. Definition of selected axes and the phase speed ratio (r_{PH}) as a surface function on Meshes 1 and 2 for the RT_0–P_0, RT_0–P_1, P_1^{NC}–P_1, BDM_1–P_0, and BDM_1–P_1 pairs.

DOI: 10.1002/fld

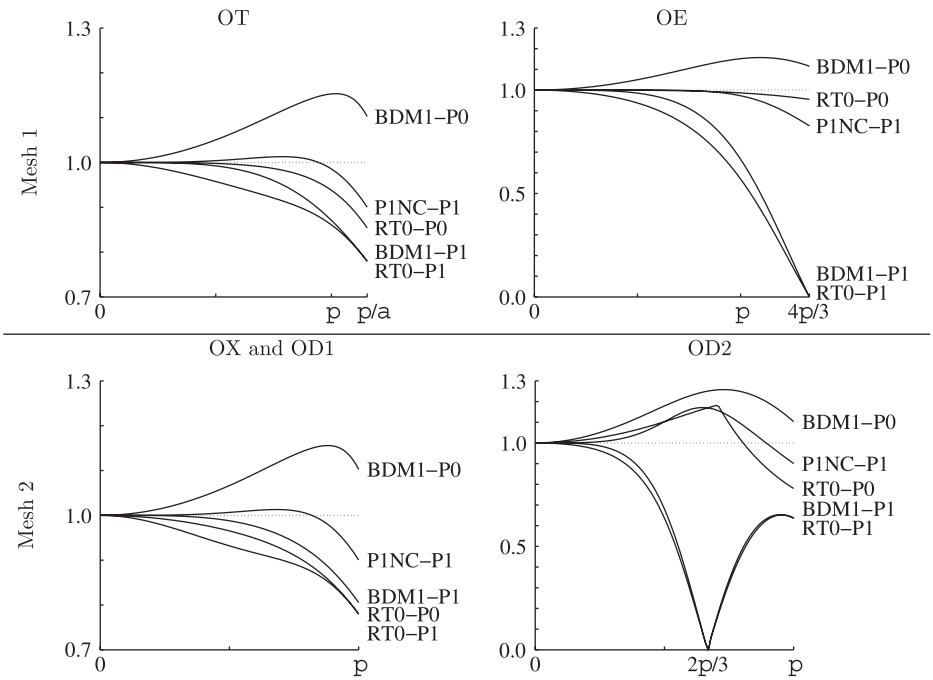

Figure 9. The phase speed ratio (r_{PH}) along selected axes in function of the normalized wave number.

Table II. Normalized wave number relations for the selected axes defined in Figure 8.

Mesh 1	Mesh 2
OE: $lh=0$ or $kh=\pm(2\alpha/3)lh$	OX: $lh=0$ or $kh=0$
OT: $kh=0$ or $kh=\pm 2\alpha lh$	OD1: $kh=lh$
	OD2: $kh=-lh$

For the RT_0–P_1 and BDM_1–P_1 pairs we have $r_{\mathrm{PH}}\leqslant 1$ for all values of kh and lh on both meshes. Furthermore, we have $r_{\mathrm{PH}}=0$ for

$$(kh,lh)=\left(\pm\frac{4\pi}{3},0\right),\left(\pm\frac{2\pi}{3},\pm\frac{\pi}{\alpha}\right)\quad\text{on Mesh 1} \tag{37}$$

$$(kh,lh)=\pm\left(\frac{2\pi}{3},-\frac{2\pi}{3}\right)\quad\text{on Mesh 2} \tag{38}$$

The wave numbers in (37) and (38) correspond to spurious surface-elevation modes introduced by the spatial discretization scheme and they are represented in Figure 10. These modes do not propagate but are trapped within the model grid which usually leads to noisy solutions. For the BDM_1–P_0 we observed that $r_{\mathrm{PH}}\geqslant 1$ on Mesh 1 for values of kh and lh inside the hexagonal area

DOI: 10.1002/fld

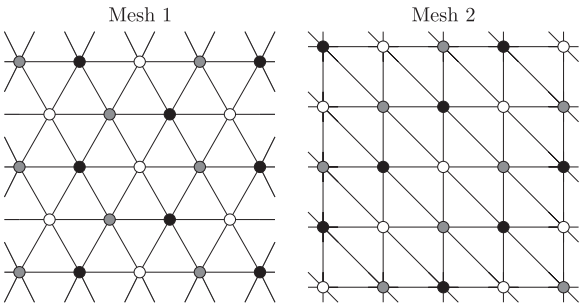

Figure 10. Zero frequency surface-elevation modes for the RT_0–P_1 and BDM_1–P_1 pairs: Mesh 1 (left) and Mesh 2 (right).

defined by the six points in (37). On Mesh 2 we have $r_{PH} \geqslant 1$ for all kh and lh values. Consequently, the gravity waves always accelerate with such a discretization scheme.

4.5. Canal simulation

In this test, Equations (1) and (2) are solved using $f = 0$. The purpose of the experiment is to validate the analytical results obtained in Section 4.4 on Mesh 2 in the OX and OD2 directions. For the OX direction, Mesh 2 is considered while in the OD2 direction we employ a mesh obtained from Mesh 2 by a rotation of $\pi/4$ as in [18, Figure 5.1]. The domain extent is $2000\,\text{km} \times 280\,\text{km}$. The resolution is set to $h = 10\,\text{km}$. The fluid is initially at rest and zero normal velocity is specified at the boundaries, except at the western one. On the western side, the fluid velocity is set to $0.1\,\text{m}\,\text{s}^{-1}$ inbound and $\eta = 1\,\text{m}$, with $H = 1000\,\text{m}$ and $g = 10\,\text{m}\,\text{s}^{-2}$, i.e. the phase speed of gravity waves is $\sqrt{gH} = 100\,\text{m}\,\text{s}^{-1}$. The Crank–Nicolson scheme is used for time discretization. The time step is set to 10 s and the gravitational Courant number is thus 0.1, such that the time step has no significant impact on the wave dispersion. The duration of the simulation is 1000 time steps and the wave front should be located at midbasin, i.e. at 1000 km from the western boundary, at the end of the simulation.

In Figure 11 the numerical solutions obtained for all FE pairs are shown for both OX and OD2 directions. The results for the P_1^{NC}–P_1 and RT_0–P_0 pairs are identical to those displayed in [18] and they are reproduced here for comparison purposes with the other pairs. The RT_0–P_1 pair exhibits the strongest oscillations trailing behind the front in both directions, while the region ahead of the front is free of oscillations. This result is in good agreement with the analysis conducted in Section 4.4 where $r_{PH} \leqslant 1$. Small oscillations appearing at the beginning of the simulation travel about two times as fast as the front and they are observed at the eastern part of the domain in Figure 11. The presence of these oscillations is beyond the scope of our analysis. The results for the BDM_1–P_1 and RT_0–P_1 pairs are similar but the amplitude of the oscillations behind the front is slightly smaller for the BDM_1–P_1 pair. The results for the BDM_1–P_0 pair show oscillations travelling faster than the wave front while the region behind the front is noise free. Again these results are in good agreement with those of Section 4.4 because $r_{PH} \geqslant 1$ in the OX and OD2 directions for all kh and lh.

The experiment has also been performed on Mesh 1 in the OE and OT directions but the results are not presented here as they are very similar to those obtained on Mesh 2.

DOI: 10.1002/fld

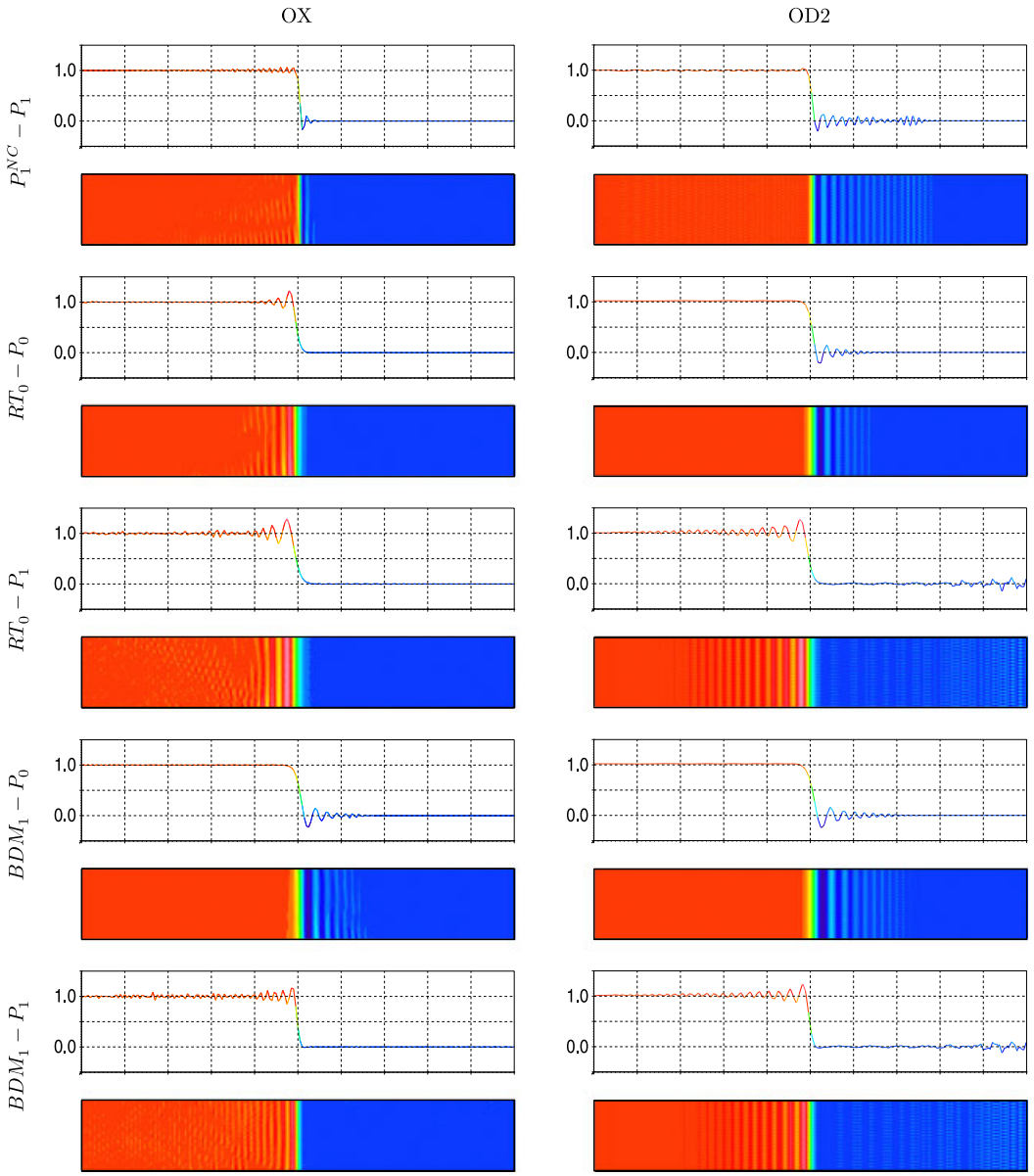

Figure 11. Surface elevation for the canal test after 10 000 s of simulation on Mesh 2.

5. GEOSTROPHIC BALANCE

5.1. *Kernel analysis*

In this analysis we seek stationary solutions to the SW systems (4) and (5) as done in [22] for the P_0–P_1, P_1^{NC}–P_1, P_1–P_1, MINI, P_1 iso P_2–P_1, and P_2–P_1 pairs. Here, we examine the RT_0–P_1,

DOI: 10.1002/fld

Table III. Dimension of the discrete operator kernels and Λ on an $n \times n$ regular Mesh 2 with no-normal flow boundary condition.

	P_1^{NC}–P_1	RT_0–P_0	RT_0–P_1	BDM_1–P_0	BDM_1–P_1
p	$6n^2$	$3(n-\frac{1}{3})^2-\frac{1}{3}$	$3(n-\frac{1}{3})^2-\frac{1}{3}$	$6(n-\frac{1}{3})^2-\frac{2}{3}$	$6(n-\frac{1}{3})^2-\frac{2}{3}$
q	$(n+1)^2$	$2n^2$	$(n+1)^2$	$2n^2$	$(n+1)^2$
$\underline{C}$	0	$(n-1)^2+1$	$(n-1)^2+1$	$2(n-1)^2+2$	$2(n-1)^2+2$
$\underline{G}$	1	1	3	1	3
$\underline{D}$	$5(n-\frac{1}{5})^2-\frac{1}{5}$	$(n-1)^2$	$2(n-1)^2$	$4(n-\frac{1}{2})^2$	$5(n-\frac{3}{5})^2+\frac{1}{5}$
$\underline{CD}$	0	0	$(n-1)^2$	$2(n-1)^2+1$	$2(n-1)^2+1$
$\underline{CG}$	$(n+1)^2$	$2n^2$	$2n^2+2$	$4(n-\frac{1}{2})^2+2$	$3(n-\frac{1}{3})^2+\frac{11}{3}$
$\underline{CDG}$	$(n-1)^2+1$	$(n-1)^2+1$	$2(n-1)^2+3$	$4(n-\frac{1}{2})^2+1$	$3(n-\frac{1}{3})^2+\frac{8}{3}$
Λ	$(n-1)^2$	$(n-1)^2$	$(n-1)^2$	$2n^2-2$	$(n+1)^2-4$

BDM_1–P_0, and BDM_1–P_1 pairs. Stationary solutions are obtained by substituting $\omega=0$ in (9) and (10) and this leads to

$$\begin{pmatrix} \underline{C} & \underline{G} \\ \underline{D} & 0 \end{pmatrix} \begin{pmatrix} \underline{\mathbf{u}} \\ \underline{\eta} \end{pmatrix} = 0 \tag{39}$$

The stationary solutions thus belong to the kernel of the matrix in the left-hand side of (39) denoted by $\underline{CDG}$. We also define

$$\underline{CD} \equiv \begin{pmatrix} \underline{C} \\ \underline{D} \end{pmatrix}, \quad \underline{CG} \equiv (\underline{C} \;\; \underline{G}) \tag{40}$$

We consider a square domain with no-normal flow boundary condition and the regular $n \times n$ Mesh 2. The dimension of the $\underline{C}$, $\underline{D}$, $\underline{G}$, $\underline{CD}$, $\underline{CG}$, and $\underline{CDG}$ matrix kernels are computed numerically using MATLAB for $n=3,\ldots,14$, and the results are extrapolated for any integer n and are given in Table III. We observe that the $\underline{C}$ matrix has a nontrivial kernel for the RT_0 and the BDM_1 elements. For the latter the kernel dimension is twice greater than the RT_0 one. The rank deficiency for the $\underline{C}$ matrix is a consequence of using only one velocity component at the velocity nodes as for the Arakawa C-grid [26, 27]. For the P_1^{NC}–P_1 pair, both velocity components are used at velocity nodes and the $\underline{C}$ matrix is thus full rank.

We note that the dimension of the $\underline{G}$ matrix kernel is equal to 1 for the P_1^{NC}–P_1, RT_0–P_0, and BDM_1–P_0 pairs. This solution corresponds to the hydrostatic surface-elevation mode, i.e. the solution with constant elevation and zero velocity. It can be simply considered as a constant of integration associated with the solution of the governing equations. However, for the RT_0–P_1 and BDM_1–P_1 pairs the dimension of the $\underline{G}$ matrix kernel is equal to 3 and hence two spurious surface-elevation modes are present.

DOI: 10.1002/fld

The dimension of the $\underline{D}$ matrix kernel can be deduced from (18) and by using the rank theorem we obtain

$$\dim(\ker(\underline{D})) = p - q + \dim(\ker(\underline{G})) \tag{41}$$

The $\underline{CD}$ matrix kernel is the intersection of the $\underline{C}$ and $\underline{D}$ matrix kernels. For the P_1^{NC}–P_1 and RT_0–P_0 pairs this intersection is empty. The dimension of the $\underline{CD}$ matrix kernel is $(n-1)^2$ for the RT_0–P_1 pair while it is twice greater for the BDM_1–P_0 and BDM_1–P_1 pairs as shown in Table III.

The modes lying in the $\underline{CD}$ matrix kernel, named here as *CD*-modes, behave similar to the spurious surface-elevation modes but they belong to the velocity space instead. The fact that the number of *CD*-modes is $O(n^2)$ compared with $O(1)$ for the spurious surface-elevation modes suggests that the *CD*-modes may appear locally on the mesh which is usually not the case for the elevation modes.

The $\underline{C}$ matrix is skew symmetric and by using (18) and the rank theorem we deduce

$$\dim(\ker(\underline{CG})) = q + \dim(\ker(\underline{CD})) \tag{42}$$

The $\underline{CDG}$ matrix kernel contains all stationary modes by definition, including the hydrostatic mode, possible spurious surface elevation and *CD*-modes. It also contains other modes that are solution of the discrete geostrophic balance, i.e. the balance between the Coriolis and the pressure gradient operators. The number of such modes is given by

$$\Lambda \equiv \dim(\ker(\underline{CDG})) - \dim(\ker(\underline{G})) - \dim(\ker(\underline{CD})) \tag{43}$$

and it is mentioned in the last line of Table III for all pairs. For the first three pairs in Table III we obtain $\Lambda = (n-1)^2$ which corresponds to the number of mesh vertices that do not lie on the boundary. For the last two pairs we have $\Lambda = 2n^2 - 2$ and $(n+1)^2 - 4$, respectively. For the first three pairs, each vertex can be associated with a smallest representable vortex (SRV) defined in [22] as the stationary solution of (39) with minimal support. As in [22], the SRV forms a basis for the discrete geostrophic balance. A typical SRV is presented in Figure 12 for the RT_0–P_1, BDM_1–P_0, and BDM_1–P_1 pairs on Meshes 2 and 3, where Mesh 3 is an unstructured mesh with smoothing. We see that the SRV structure is larger for these three pairs than for the P_1^{NC}–P_1 and RT_0–P_0 pairs examined in [22] on both meshes. Note that SRV with more complex structures also exist near the boundary for the BDM_1–P_0 and BDM_1–P_1 pairs.

5.2. Propagating eddy simulation

In this experiment our purpose is to validate the results obtained in Table III. The slowly propagating Rossby modes are simulated in the case of the evolution of a typical anticyclonic eddy at midlatitudes. The domain is a 2000 km × 1200 km rectangular basin and the triangulation has a resolution of 20 km. The β-plane approximation, $f = f_0 + \beta y$, is used where $f_0 = 6.1634 \times 10^{-5}\,\mathrm{s}^{-1}$ and $\beta = 2.0746 \times 10^{-11}\,\mathrm{m}^{-1}\,\mathrm{s}^{-1}$, and the choice $g = 9.81\,\mathrm{m\,s}^{-2}$ and $H = 1.6309\,\mathrm{m}$ results in a phase speed for gravity waves of $\sqrt{gH} = 4\,\mathrm{m\,s}^{-1}$. The radius of deformation at midbasin is $\sqrt{gH}/f_0 = 65\,\mathrm{km}$. A Gaussian distribution centered in the domain is prescribed at initial time for the elevation and the initial velocity is in geostrophic balance

$$\mathbf{u} = -2\frac{g}{f}\frac{A}{r^2}\exp\left(-\frac{|\mathbf{x}|^2}{r^2}\right)\mathbf{k}\times\mathbf{x} \tag{44}$$

DOI: 10.1002/fld

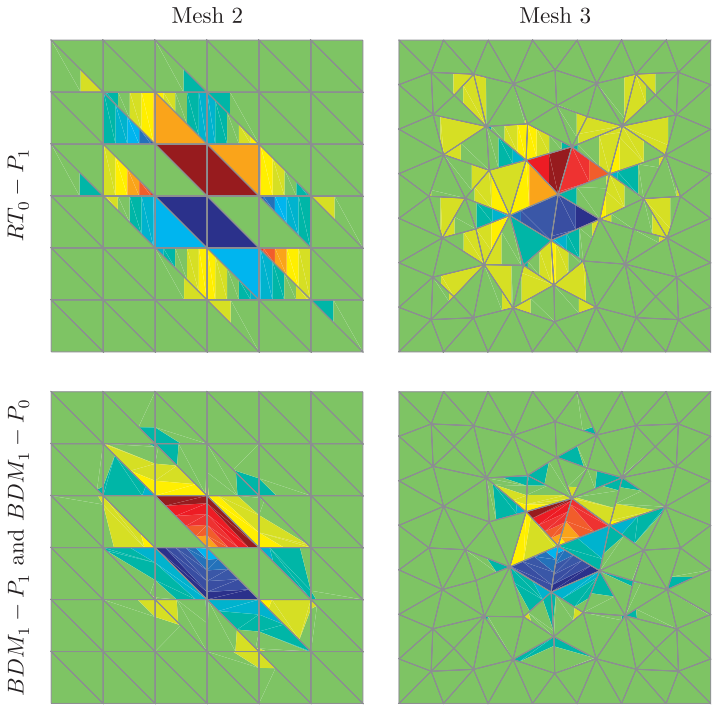

Figure 12. x-Component of the velocity for a typical RT_0–P_1, BDM_1–P_0, and BDM_1–P_1 smallest representable vortex.

$$\eta = A \exp\left(-\frac{|\mathbf{x}|^2}{r^2}\right) \tag{45}$$

where $r = 1.3 \times 10^5$ m and $A = 0.95$ m. The Crank–Nicolson scheme is again used and the time step is set to 1800 s. The vortex moves slowly westward as predicted by the Rossby wave dynamics. Figures 13 and 14 show the surface elevation and flow speed field after 5 weeks of simulation on Mesh 2 and the unstructured Mesh 3, respectively. Note that the solutions have been linearly interpolated to represent continuous isolines.

On Mesh 2, the solution is very smooth for both the elevation and the flow speed field. The solutions are nearly identical for the five FE pairs and minor differences are barely observed. On Mesh 3, the surface elevation and flow speed field are very similar to those obtained on Mesh 2 in Figure 13 for the P_1^{NC}–P_1, RT_0–P_0, and RT_0–P_1 pairs. However, for the BDM_1–P_0 and BDM_1–P_1 pairs the situation is very different. Indeed, the flow speed field exhibits severe oscillations that lead to unstable results. The observed oscillations appear early in the simulation after only few time steps and gradually grow in time. Although the oscillations in the flow speed field rapidly increase, the surface elevation remains coherent with the presence of mild oscillations. We suspect that the presence of *CD*-modes in Table III might be responsible for the oscillations observed in Figure 14 for the BDM_1–P_0 and BDM_1–P_1 pairs. In that case the *CD*-modes, although present, are not triggered by the use of an unstructured mesh for the RT_0–P_1 pair.

DOI: 10.1002/fld

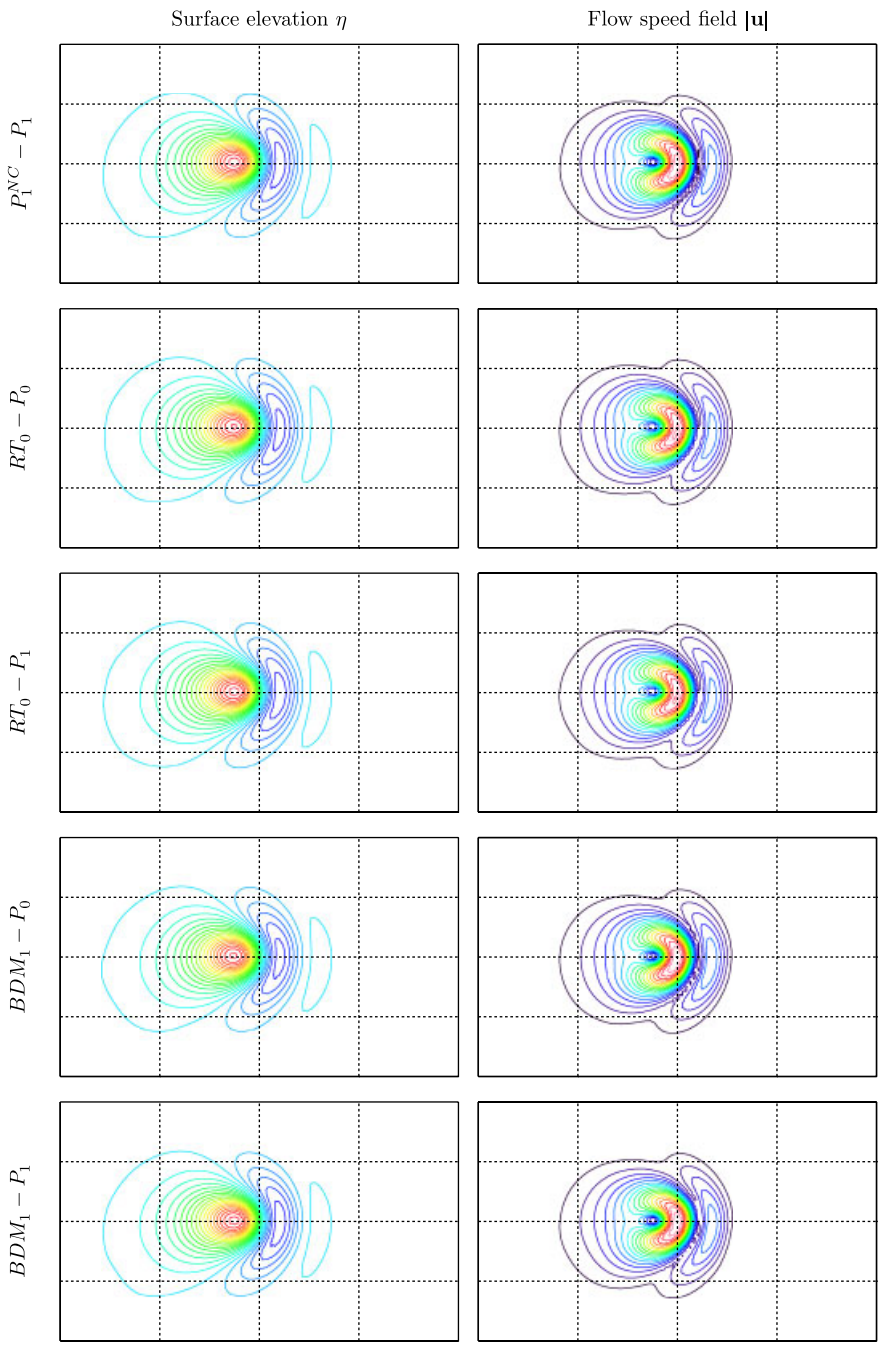

Figure 13. Surface elevation and flow speed field after 5 weeks of simulation on Mesh 2.

DOI: 10.1002/fld

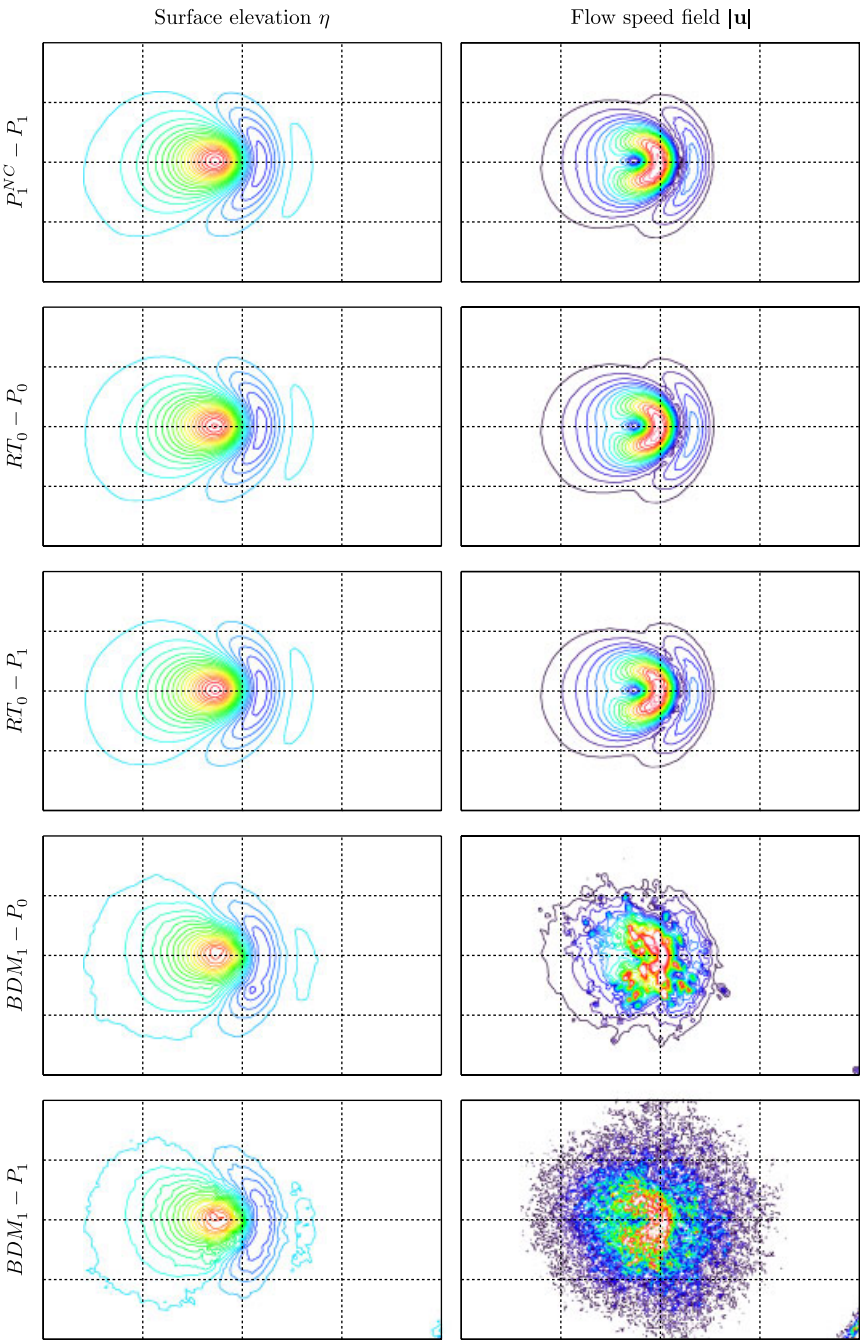

Figure 14. As for Figure 13 but on Mesh 3.

DOI: 10.1002/fld

6. CONCLUSION

An analysis of the Raviart–Thomas and Brezzi–Douglas–Marini FE pairs is presented to determine the ability of these pairs in solving the SW equations. An inertia–gravity wave dispersion analysis is performed on meshes made up of equilateral and right biased triangles. Spurious surface elevation modes are observed for the RT_0–P_1 and BDM_1–P_1 pairs. The analysis also permits to show that the RT_0–P_0 and P_1^{NC}–P_1 pairs have the lowest amount of dispersion on both meshes compared with the RT_0–P_1, BDM_1–P_0, and BDM_1–P_1 ones. We note that solutions on equilateral meshes present less dispersion than on meshes made up of right biased triangles. The simulation results of a gravity wave propagating in a canal are in good agreement with the analytical computations. The geostrophic equilibrium is investigated through a linear algebra kernel computation approach. Such an analysis shows the presence of spurious *CD*-modes in the velocity space for the RT_0–P_1, BDM_1–P_0, and BDM_1–P_1 pairs. SRV structures have been computed for all pairs and compared with the RT_0–P_0 and P_1^{NC}–P_1 ones on both structured and unstructured meshes. Numerical solutions of a propagating eddy at midlatitudes give smooth elevation and flow speed field on the uniform mesh for all pairs. These results still hold for the P_1^{NC}–P_1, RT_0–P_0, and RT_0–P_1 pairs on the unstructured triangulation while unstable results are obtained for the BDM_1–P_0 and BDM_1–P_1 pairs in the representation of the flow speed field only. We suspect the *CD*-modes to be responsible for this behavior.

ACKNOWLEDGEMENTS

This work is supported by grants from the Natural Sciences and Engineering Research Council (NSERC) and FQRNT (Fonds Québécois de la Recherche sur la Nature et les Technologies). The numerical codes make use of SPARSKIT [28] and GMSH [29].

REFERENCES

1. Carey GF (ed.). *Finite Element Modeling of Environmental Problems*. Wiley: New York, 1995.
2. Danilov S, Kivman G, Schröter J. A finite-element ocean model: principles and evaluation. *Ocean Modelling* 2004; **6**:125–150.
3. Hua B, Thomasset F. A noise-free finite-element scheme for the two-layer shallow water equations. *Tellus* 1984; **36**:157–165.
4. Le Provost C, Vincent P. Finite element for modeling ocean tides. In *Tidal Hydrodynamics*, Parker B (ed.). Wiley: New York, 1991; 41–60.
5. Le Roux DY, Staniforth A, Lin CA. Finite element for shallow-water equation ocean models. *Monthly Weather Review* 1998; **126**:1931–1951.
6. Hanert E, Legat V, Deleersnijder E. A comparison of three finite elements to solve the linear shallow water equations. *Ocean Modelling* 2002; **5**:17–35.
7. Lynch D, Gray W. A wave-equation model for finite-element tidal computations. *Computers and Fluids* 1979; **7**:207–228.
8. Côté J, Staniforth A. An accurate and efficient finite-element global model of the shallow-water equations. *Monthly Weather Review* 1990; **118**:2707–2717.
9. Le Roux DY, Lin CA, Staniforth A. A semi-implicit semi-Lagrangian finite-element shallow-water ocean model. *Monthly Weather Review* 2000; **128**:1384–1401.
10. Walters RA, Cheng RT. Accuracy of an estuarine hydrodynamic model using smooth elements. *Water Resources Research* 1980; **16**:187–195.
11. Agoshkov V, Ovtchinnikov E, Pennati V, Ambrosi D, Saleri F. Finite element, finite volume, and finite differences approximation to the shallow water equations. In *Finite Elements in Fluids*, Morgan K, Oñate E, Periaux J, Peraire J, Zienkiewicz OC (eds). Pineridge Presso: Barcelona, Spain, 1993; 1001–1009.

DOI: 10.1002/fld

12. Iskandarani M, Haidvogel D, Boyd J. A staggered spectral finite-element model for the shallow-water equations. *International Journal for Numerical Methods in Fluids* 1995; **20**:393–414.
13. Williams RA, Zienkiewicz OC. Improved finite-element forms for the shallow-water wave equations. *International Journal for Numerical Methods in Fluids* 1981; **1**:81–97.
14. Kinnmark IP, Gray WG. A two-dimensional analysis of the wave equation model for finite element tidal computations. *International Journal for Numerical Methods in Engineering* 1984; **20**:369–383.
15. Hughes TJR, Franca LP, Balestra M. A new finite element formulation for computational fluid dynamics: V. Circumventing the Babuška–Brezzi condition: a stable Petrov–Galerkin formulation of the Stokes problem accommodating equal-order interpolations. *Computer Methods in Applied Mechanics and Engineering* 1986; **59**: 85–99.
16. Le Roux DY, Carey GF. Stability/dispersion analysis of the discontinuous Galerkin linearized shallow-water system. *International Journal for Numerical Methods in Fluids* 2005; **48**:325–347.
17. Le Roux DY. Dispersion relation analysis of the P_1^{NC}–P_1 finite element pair in shallow-water ocean models. *SIAM Journal on Scientific Computing* 2005; **27**:394–414.
18. Le Roux DY, Rostand V, Pouliot B. Analysis of numerically-induced oscillations in 2D finite-element shallow-water models, part I: inertia–gravity waves. *SIAM Journal on Scientific Computing* 2007; **29**:331–360.
19. Le Roux DY, Pouliot B. Analysis of numerically-induced oscillations in 2D finite-element shallow-water models, part II: free planetary waves. *SIAM Journal on Scientific Computing*, submitted.
20. Walters RA, Carey GF. Analysis of spurious oscillation modes for the shallow water and Navier–Stokes equations. *Computers and Fluids* 1983; **11**:51–68.
21. Le Roux DY, Sène A, Rostand V, Hanert E. On some spurious mode issues in shallow-water models using a linear algebra approach. *Ocean Modelling* 2005; **10**:83–94.
22. Rostand V, Le Roux DY, Carey GF. Kernel analysis of the discretized finite difference and finite element shallow-water models. *SIAM Journal on Scientific Computing*, submitted.
23. Brezzi F, Douglas J, Marini LD. Recent results on mixed finite element methods for second order elliptic problems. In *Vistas in Applied Mathematics*, *Numerical Analysis*, *Atmospheric Sciences*, *Immunology*, Balakrishanan AV, Dorodnitsyn AA, Lions JL (eds). Optimization Software Inc.: New York, 1986.
24. LeBlond PH, Mysak LA. *Waves in the Ocean*. Elsevier: Amsterdam, 1978.
25. Foreman MGG. A two-dimensional dispersion analysis of selected methods for solving the linearized shallow-water equations. *Journal of Computational Physics* 1984; **56**:287–323.
26. Adcroft AJ, Hill CN, Marshall J. A new treatment of the coriolis term in C-grid models at both high and low resolutions. *Monthly Weather Review* 1999; **127**:1928–1936.
27. Mesinger F, Arakawa A. *Numerical Methods Used in Atmospheric Models*. Garp Publications, 1976.
28. Saad Y. SPARSKIT: a basic tool kit for sparse matrix computations, 2005. http://www.cs.umn.edu/~saad/software/SPARSKIT/sparskit.html.
29. Geuzaine C, Remacle JF. GMSH: a three-dimensional finite element mesh generator with built-in pre- and post-processing facilities, 2007. http://www.geuz.org/gmsh/.

DOI: 10.1002/fld